Research Article

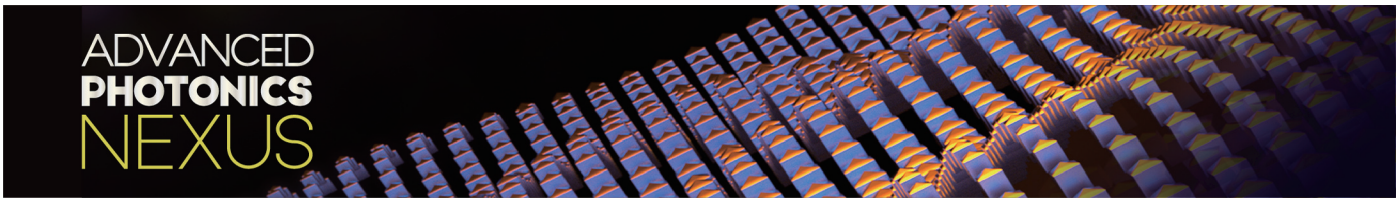

Flexible depth-of-focus, depth-invariant resolution photoacoustic microscopy with Airy beam

Wangting Zhou,[a,b,c,d] Hui Xie,[a,b,c] Kezhou Li,[a,b,c] Zhiyuan Sun,[a,b,c] Jiangshan He,[a,b,c] Zhen Yuan,[e] Xunbin Wei,[f,g,h,*] and Xueli Chen[a,b,c,d,*]

[a]Xidian University, School of Life Science and Technology, Center for Biomedical-photonics and Molecular Imaging, Advanced Diagnostic-Therapy Technology and Equipment Key Laboratory of Higher Education Institutions in Shaanxi Province, Xi'an, China
[b]Xidian University, School of Life Science and Technology, International Joint Research Center for Advanced Medical Imaging and Intelligent Diagnosis and Treatment, Xi'an Key Laboratory of Intelligent Sensing and Regulation of trans-Scale Life Information, Xi'an, China
[c]Xidian University, Ministry of Education, Engineering Research Center of Molecular and Neuro Imaging, Xi'an, China
[d]Xidian University, Guangzhou Institute of Technology, Innovation Center for Advanced Medical Imaging and Intelligent Medicine, Guangzhou, China
[e]University of Macau, Faculty of Health Sciences, Macau, China
[f]Peking University Cancer Hospital & Institute, Ministry of Education, Laboratory of Carcinogenesis and Translational Research, Beijing, China
[g]Peking University, Biomedical Engineering Department, Beijing, China
[h]Peking University Health Science Center, Institute of Medical Technology, Beijing, China

Abstract. Optical-resolution photoacoustic microscopy (OR-PAM) has rapidly developed and is capable of characterizing optical absorption properties of biological tissue with high contrast and high resolution (micrometer-scale lateral resolution). However, the conventional excitation source of rapidly diverging Gaussian beam imposes limitations on the depth of focus (DOF) in OR-PAM, which in turn affects the depth-resolving ability and detection sensitivity. Here, we proposed a flexible DOF, depth-invariant resolution photoacoustic microscopy (FDIR-PAM) with nondiffraction of Airy beams. The spatial light modulator was incorporated into the optical pathway of the excitation source with matched switching phase patterns, achieving the flexibly adjustable modulation parameters of the Airy beam. We conducted experiments on phantoms and intravital tissue to validate the effectiveness of the proposed approach for high sensitivity and high-resolution characterization of variable topology of tissue, offering a promising DOF of 926 μm with an invariant lateral resolution of 3.2 μm, which is more than 17-fold larger compared to the Gaussian beam. In addition, FDIR-PAM successfully revealed clear individual zebrafish larvae and the pigment pattern of adult zebrafishes, as well as fine morphology of cerebral vasculature in a large depth range with high resolution, which has reached an evident resolving capability improvement of 62% mean value compared with the Gaussian beam.

Keywords: flexible depth of focus; Airy beam; photoacoustic microscopy; invariant lateral resolution.

Received Mar. 18, 2024; revised manuscript received Apr. 17, 2024; accepted for publication May 6, 2024; published online May 24, 2024.

[DOI: 10.1117/1.APN.3.4.046001]

1 Introduction

Optical-resolution photoacoustic microscopy (OR-PAM), as an emerging and hybrid technique, enables label-free and *in vivo* anatomical as well as functional imaging of the microvasculature, lipids, and melanin in biological tissue with deep penetration.[1–5] OR-PAM inherently possesses the depth-resolving capacity, utilizing the time-of-flight data captured in each photoacoustic signal during A-scan excitation. This unique feature allows for volumetric imaging with only two-dimensional (2D) raster scanning. To achieve optical-diffraction-limited lateral resolution, a tightly focused Gaussian beam is selected using an optical objective in a standard OR-PAM system.[2–7] Nevertheless, the diffraction limit causes the commonly used Gaussian beam to rapidly diverge along its propagation path,

*Address all correspondence to Xueli Chen, xlchen@xidian.edu.cn; Xunbin Wei, xwei@bjmu.edu.cn

resulting in a notably brief depth of focus (DOF) for exciting photoacoustic signals. This restricted DOF prevents the consistent revelation of volumetric images with uniform lateral resolution across varying depths, thus hindering the accurate acquisition of anatomical, functional, and metabolic information concerning biological systems.

Recently, a needle-shaped beam was utilized in photoacoustic microscopy to extend the DOF using customized diffractive optical components, as well as a transparent microfiber Fabry–Perot ultrasound sensor with a needle-shaped focus for multiscale photoacoustic imaging. However, the achieved efficiency is ~30% of the input beam energy, and the DOF remains relatively fixed, due to a fabricated phase pattern, limiting its versatility across various imaging application scenarios.[8,9] Zhao et al. designed a millimeter-scale UV metalens based on the extended Nijboer–Zernike wavefront-shaping theory, which effectively extends the DOF of a UV-PAM system. Nonetheless, the ability to flexibly modulate DOF still encounters limitations when faced with complex application scenarios.[10] Other methods attempt to extend the DOF for deep-range imaging, including digital focusing, spatial and spectral multiplexing, wavefront correction, and Bessel beams. Digital focusing[11] uses a light source with high phase stability throughout the whole imaging process. However, the resolution enhancement is limited in dense samples such as human skin because of the large difference between the spherical wavefront employed in the refocusing model and the practical wavefronts, which are highly disturbed by the sample itself. Spatial and spectral multiplexing techniques have been used in multiplane microscopes.[12–14] However, when conducting three-dimensional (3D) multiplane mapping, it is crucial to accurately calibrate the image plane for preprocessing due to the susceptibility to misalignment of detection channels. In contrast, Fourier ptychographic microscopy utilizes a straightforward configuration and implements a wavefront correction strategy to enhance the DOF.[15] Nonetheless, the imaging reconstruction method of Fourier ptychographic microscopy relies on the use of oblique plane waves to illuminate thin sample targets, restricting its suitability for intravital mapping of thick tissues. In addition, propagation-invariant beam fields, such as Bessel beams and structured illumination, can enhance the DOF without sacrificing its focal size.[16–20] However, Bessel beam-based approaches usually reclaim contrast because of the transversal outer ring that could produce background artifacts and preclude better axial resolution.[21–23] On the other hand, a Bessel beam possesses only a small fraction of power in its central lobe (with a sidelobe to central-mail lobe ratio reaching up to merely 20%) that may affect its sensitivity and image quality.[24] Using a structured illumination in PAM usually limits its imaging speed because a series of propagation-invariant sinusoidal fringes need to be applied, and complicated postprocessing procedures are also required. In summary, PAM needs a solution performing a large DOF gain, a uniform beam profile with high-sensitivity, fewer sidelobe artifacts, and good system compatibility.

To satisfy these requirements, we propose a flexible DOF, depth-invariant resolution photoacoustic microscopy (FDIR-PAM), achieved through the finite energy Airy beam as the excitation source of photoacoustic signals. The nondiffraction of the Airy beam can effectively mitigate the trade-off between DOF and lateral light diffraction, thus providing a substantially improved DOF equipped with a depth-invariant resolution. In addition, the central-main lobe of the Airy beam carries a relatively higher amount of energy (>50%) when the decaying factor is ~0.11, and provides a longer DOF with flexible modulation of central-main lobe structure.[25–31] The FDIR-PAM system also provides the flexibility to adjust the trade-off between DOF and sensitivity by simply switching the scale factor. This adjustment is easily achieved through cubic phase modulations of Gaussian beams cooperating with a spatial light modulator (SLM). Furthermore, compared to structured illumination methods, FDIR-PAM eliminates the need for applying a series of sinusoidal fringes and complicated postprocessing techniques. We successfully demonstrate the application of FDIR-PAM in mapping various topological structures and performing large volumetric characterization without the need for depth-direction scanning. Notably, we showcase the imaging of zebrafish larvae and adults at different developmental stages using visible FDIR-PAM, and we also acquire the intravital characterization of mouse's cerebral vasculature to highlight the potential clinical applications of this proposed method.

2 Methods

2.1 Principle and Simulation

By introducing a cubic phase into a basic Gaussian beam, the generation of an Airy beam is made possible. The behavior of optical Airy wave packets can be characterized by the potential-free Schrödinger equation under paraxial conditions, following the diffraction relation,[25]

$$i\frac{\partial \phi}{\partial \xi}+\frac{1}{2}\frac{\partial^2 \phi}{\partial s^2}=0. \tag{1}$$

Here, the dimensionless transverse coordinate is represented by $s=x/x_0$, an arbitrary transverse scale is denoted by x_0, and the electric field envelope is denoted by ϕ. $\xi=z/k_0^2$ denotes a normalized propagation distance. To obtain the envelope of a finite Airy beam, the normalized paraxial equation of diffraction is solved by performing an exponential aperture function, resulting in Refs. 25 and 32,

$$\begin{aligned}\phi(s,\xi)=Ai[s-(\xi/2)^2+ia\xi]\exp\{as-[a\xi^2/2-i(\xi^3/12)]\\+i(a^2\xi/2)+i(s\xi/2)\},\end{aligned} \tag{2}$$

where the Airy function is represented by $Ai[s-(\xi/2)^2+ia\xi]$, parameter a ensures containment of the infinite Airy tail, and a is significantly <1. Here, the normalized propagation distance is denoted by $\xi=z/kx_0^2$, the wavenumber of the optical wave is represented by $k=2\pi n/\lambda$, n denotes the refractive index of the medium, and λ represents the free-space wavelength. In practical applications, the finite-energy Airy beams with an exponentially decaying version can be expressed as[32]

$$\phi(s,\xi=0)=Ai(s)\exp(as). \tag{3}$$

The mathematical expression of the Airy beam in normalized k-space is derived by taking the Fourier transform of Eq. (3), with its Fourier spectrum given as[32]

$$\phi(k)=\exp(-ak^2)\exp\left[\frac{i}{3}(k^3-3a^2k-ia^3)\right]. \tag{4}$$

Through an analysis of the propagation features of finite-energy Airy wave packets, it can be observed that the Fourier transform of function $Ai(s)\exp(as)$ results in a Gaussian beam that is modulated with a cubic phase (k^3). Specifically, the cubic phase spectrum for a 2D Airy beam can be represented as $\varphi_{AB}(k_x, k_y) = [i\beta^3(k_x^3 + k_y^3)/3]$, where kx and ky denote the Fourier spectrum coordinates, and β represents the scale factor.[33] This cubic phase spectrum is shown in Fig. 1. Thus, by applying a cubic phase modulation and focusing the resulting beam with a Fourier objective lens to give a Fourier transformation, a linearly polarized Gaussian beam can be converted into an Airy beam. Supplementary Material Note 1 contains simulation results that illustrate the beam intensity distribution and propagation properties of both the Gaussian and Airy beams. Correlation analysis shows that PAM based on Airy beam excitation can extend the DOF with relatively ideal resolution. In order to further characterize the influence of different phase modulation parameters on Airy beam property, we made beam simulation maps under different scale factors β; the results are present in Fig. 1. The first row of Fig. 1(a) represents the phase patterns of an Airy beam under different scale factors, and the second row is the cross-sectional maps of the spot at the focus position. It can be observed that with the increase of the scale factor, the sidelobe of the Airy beam becomes more significant, and both have relatively consistent size distribution of the focusing spot. And then, from the third and fourth rows of Fig. 1(a), with the increase of propagation distance, Airy beams with different modulation parameters have good beam focusing

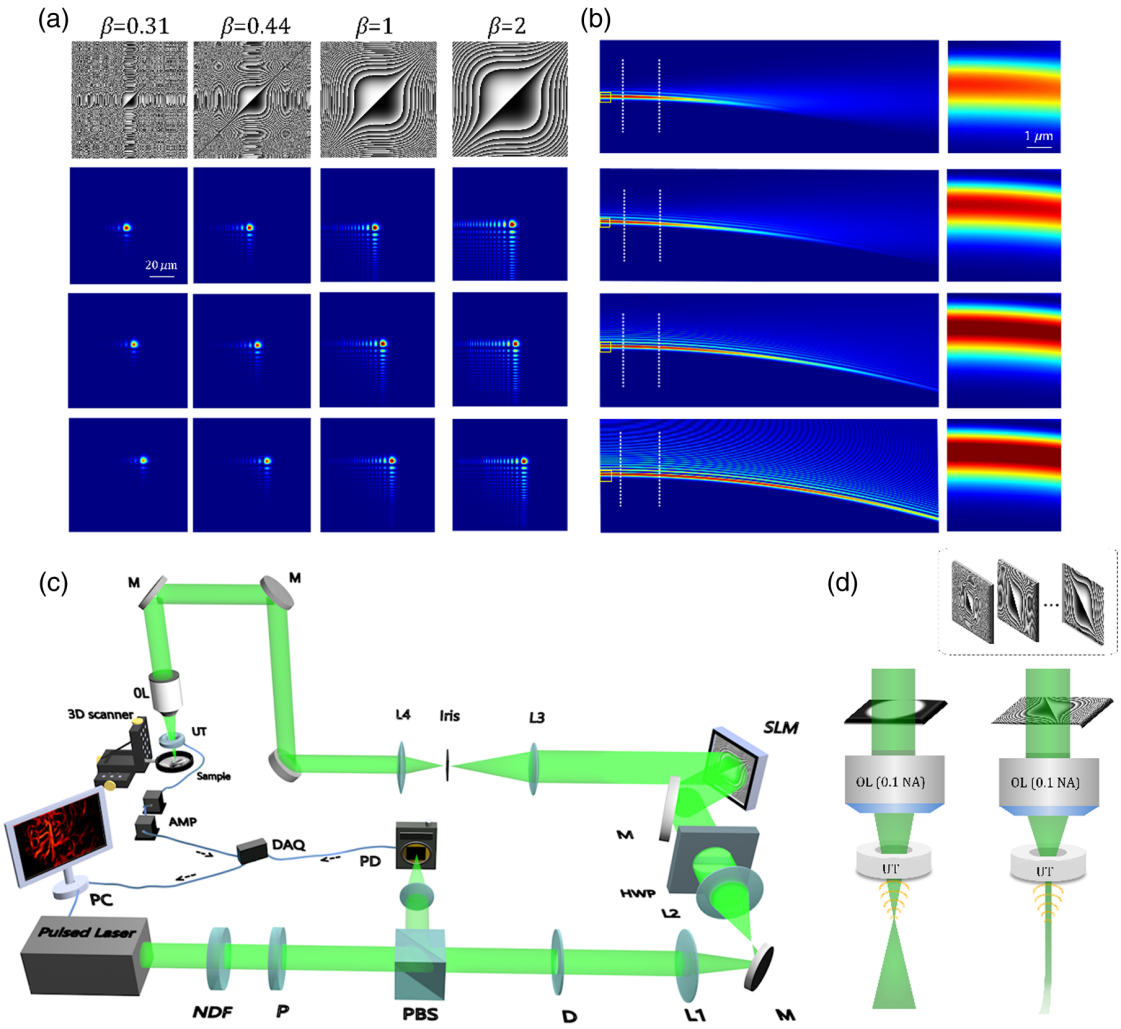

Fig. 1 Analysis of the influence of modulation parameters of Airy beam phase pattern on beam property. (a) The different phase patterns, cross-sectional beam-spot maps of xy direction at the focus position, and cross-sectional beam-spot maps of xy direction at the defocus position, respectively. (b) Left column: beam propagation property maps in the xz direction that correspond to the different modulation parameters in (a); right column: zoom-in maps of the initial beam intensity distribution that correspond to the yellow region in the left column. (c) and (d) Schematic diagram of flexibly adjustable FDIR-PAM using an SLM. NDF, neutral density filter; PD, photodetector; HWP, half-wave plate; PBS, polarization beam splitter; M, mirror; L1–L4, lenses; OL, objective lens; D, diaphragm; P, polarizer; SLM, spatial light modulator; UT, ultrasonic transducer; AMP, amplifier; DAQ, data acquisition card; PC, personal computer.

property. Furthermore, we analyzed the characteristics of the beam in the propagation direction under different scale factors; the results are shown in Fig. 1(b). As can be observed from the simulation results, the propagation distance of the Airy beam increases with the decrease of attenuation, but the sidelobe becomes more and more significant. In addition, it can be found that with the increase of the scale factor, the initial beam intensity of the Airy beam becomes stronger (refer to the rightmost column of Fig. 1(b), corresponding to the yellow box area of the left column).

2.2 FDIR-PAM System

In the experimental setup, we employed an SLM to introduce the cubic phase modulation at the Fourier plane of the excitation path in the FDIR-PAM system. The use of an SLM allowed us to adjust the scale factor and control the cubic phase, thereby truncating the tail of an infinite Airy beam. The experimental configuration of the FDIR-PAM setup is shown in Fig. 1(c). The excitation beam of the microscopy was from a pulsed laser (10 ns, 1 KHz, and 532 nm). During the experiment, we adjusted the laser pulse energy to 379 mW using neutral density filters (NDF, NDC-50C-2, Thorlabs Inc.). The laser energy output ratio was regulated by a polarizer (P, LPVISA100-MP2, Thorlabs) and a polarizing beam splitter (PBS, PBS201, Thorlabs Inc.), dividing the pump laser beam into two paths. One path carried a power of 2.20 μJ at 532 nm, while the other path had a power of 0.28 μJ for triggering the photodetector. To ensure efficient conversion from a basic Gaussian beam to an Airy beam, we employed half-wave plates (HWPs, WPH10E-532, Thorlabs Inc.) to control the linear polarization direction of the excitation beam before it passed through the SLM (Holoeye, PLUTO). A lens telescope comprising L1 (focal length $f1 = 30$ mm) and L2 ($f2 = 100$ mm) was used to extend the beam size and sufficiently illuminate the SLM screen. Scanning relay lenses L3 ($f3 = 100$ mm) and L4 ($f4 = 50$ mm) were employed to match the beam size with the back aperture of an objective lens (4×, 0.1 NA, UPlanSApo, Olympus) that had a working distance of 18.5 mm. The implementation of a blazed grating in combination with an iris was used to remove spurious orders of diffraction, separating the zeroth- (unmodulated) and first-order (desired) diffraction. By employing a blazed grating alongside an iris through an SLM, adjusting the iris diameter allows us to eliminate the unwanted zeroth-order spot while maintaining the intended first-order diffraction. The pulsed laser-triggered ultrasonic waves were detected and received by a ring-shaped ultrasonic transducer (UT) fixed coaxially with the optical axis of the objective lens. The characteristics of the UT include an inner diameter of 1.2 mm, outer diameter of 4.5 mm, focal length of 4.4 mm, center frequency of 50 MHz, and a 6-dB bandwidth of 90%. The detected photoacoustic (PA) signals were amplified using two 30 dB low-noise amplifiers (ZFL-500LN+, Mini-Circuits) and digitized by a data acquisition card (DAQ) with a sampling rate of 250 MS/s (PCIE-1425, Yixing Technology). For sequential control of the PA laser trigger, data acquisition, and raster scanning, we employed a controller card (Zmotion, National Instruments) programmed using LabVIEW. Figure 1(d) shows the principle of conventional Gaussian-beam excitation PAM and Airy-beam excitation PAM, respectively. This gives the representative phase patterns and the corresponding Airy beam achieved from the optical focus plane.

3 Results

3.1 Beam Profiles and Setup Performance

To characterize the optical properties of the modulated beam, we utilized a CMOS camera (CS165MU/M, Thorlabs) positioned at the back focal plane of the excitation beam to capture beam images (refer to Fig. 2). Figures 2(a)–2(c) display the different phase patterns employed in our experiments, denoted as Gaussian, Airy#1, and Airy#2 with varying scale factors. In the absence of phase modulation, the measured spot size of the Gaussian beam (full width at half-maximum, FWHM) expanded to ~26 μm at 1.5 mm beyond the focal plane of the objective lens, accompanied by a significant drop in laser fluence, as shown in Figs. 2(d) and 2(g) (note the difference in color bar ranges). Upon loading the cubic phase onto the SLM, finite-energy Airy beams were generated at the Fourier focal plane. The intensity pattern revealed a multilobed distribution [Figs. 2(e) and 2(f)], with the main lobe containing most of the total beam energy, consistent with the results of simulation experiments involving various Airy modulation depth parameters (Figs. 1 and S1 in the Supplementary Material). The main lobe FWHM of the Airy beams at the focus were ~5 and 3 μm for phase patterns #1 and #2, respectively. The scale factors of Airy beams #1 and #2 were 0.6 and 2, respectively, determining the decay rate of sidelobes along the transverse direction and the beam decay rate along the propagation direction. A larger scale factor resulted in a narrower main lobe size, higher energy carried in the main lobe with a longer DOF, and a greater total displacement of self-bending. Moreover, a smaller scale factor led to broader main lobes of the Airy beam, with the sidelobes positioned farther away from the main lobe and each other [Figs. 2(e) and 2(f)]. During the experiment, it was observed that Airy beam #2 exhibited a relatively larger DOF with more prominent sidelobes compared to Airy beam #1. In addition, the energy carried in the central-main lobe for Airy beam #2 was greater than that for Airy beam #1, with measured values of 69% and 54%, respectively [Figs. 2(k) and 2(l)]. Furthermore, the lateral resolution of FDIR-PAM was measured by imaging a USAF 1951 resolution target (Thorlabs) in Fig. 2(m). The corresponding edge spread function (ESF) was fitted according to the white dotted line of B-scan data. After taking the first derivative of the ESF, the lateral resolution was measured based on the FWHM values of the Gaussian fitting, performing a lateral resolution of 3.2 μm at the focal plane. As the sidelobes of the Airy beam existed and influenced the focusing light spot to some extent, the lateral resolution value was slightly greater than the size of the central-main lobes. Figure 2(n) depicted the depth-axial distribution of the lateral resolution, demonstrating that the system maintained a DOF of 926 μm with an invariant lateral resolution of 3.2 μm.

3.2 Flexibly Adjusting Airy Beam in Phantom Imaging

In order to assess the feasibility of FDIR-PAM in a phantom experiment, we conducted volumetric imaging of a letter phantom fixed in a mixture of 1.6% Intralipid solution and 1% agar gel. The "XD" pattern of the letter phantom was positioned in ultrasound gel at an angle along the depth direction (z axis), and raster scanning was performed on the phantom during the imaging process. Using both Gaussian- and Airy-beam modalities, we sequentially performed volumetric imaging and switched between PA excitation modalities by assigning corresponding

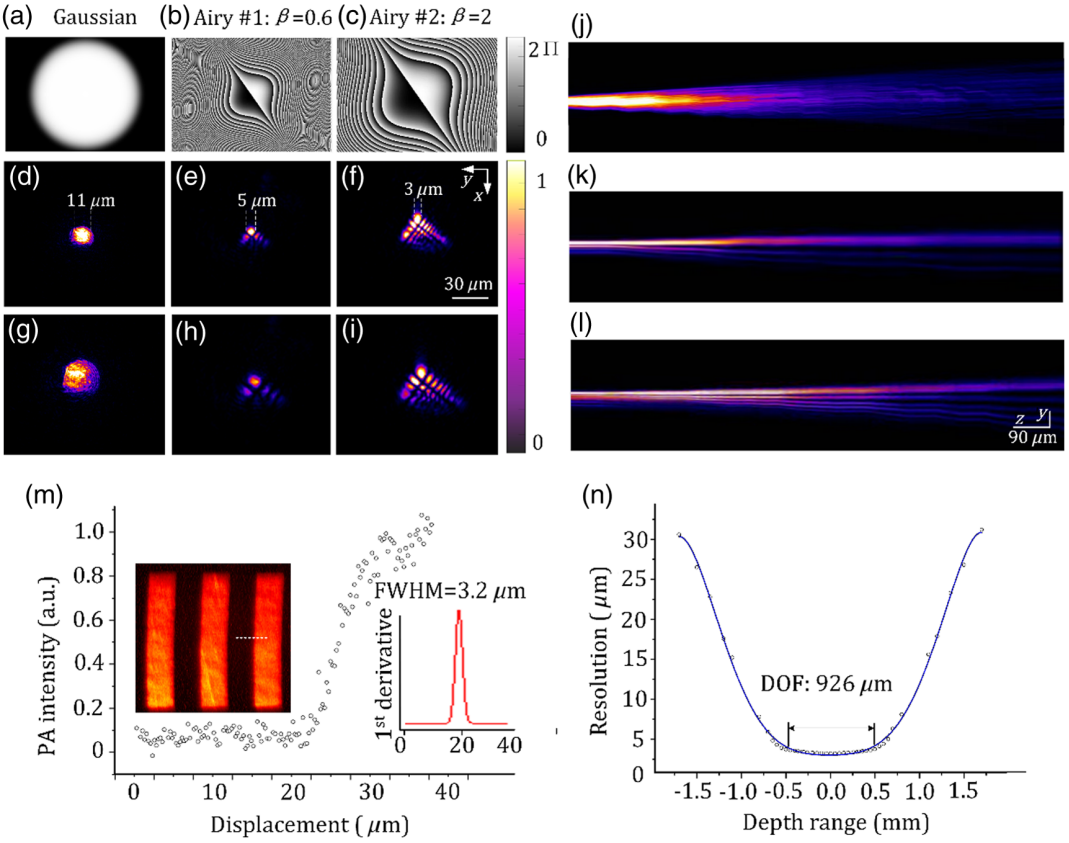

Fig. 2 Beam property characterization. (a)–(c) Phase patterns of Gaussian and Airy beams generated by SLM. (d)–(f) Measured 2D beam intensity distributions for (a) focused Gaussian, (b) Airy beam #1, and (c) Airy beam #2 at the focal plane. (g)–(h) Measured beam intensity distributions of Gaussian beam and Airy beams #1 and #2 at 1.5 mm away from the focal plane, respectively. (j)–(l) Optical intensities in the sagittal plane of Gaussian beam and Airy beams #1 and #2, respectively. The white dashed line depicts the measured FWHM. The color bar gives a linear intensity distribution. (m) Lateral resolution of the FDIR-PAM system, giving the ESFs and its first derivative extracted from the corresponding B-scan of PAM map. (n) The depth-axial distribution of lateral resolution.

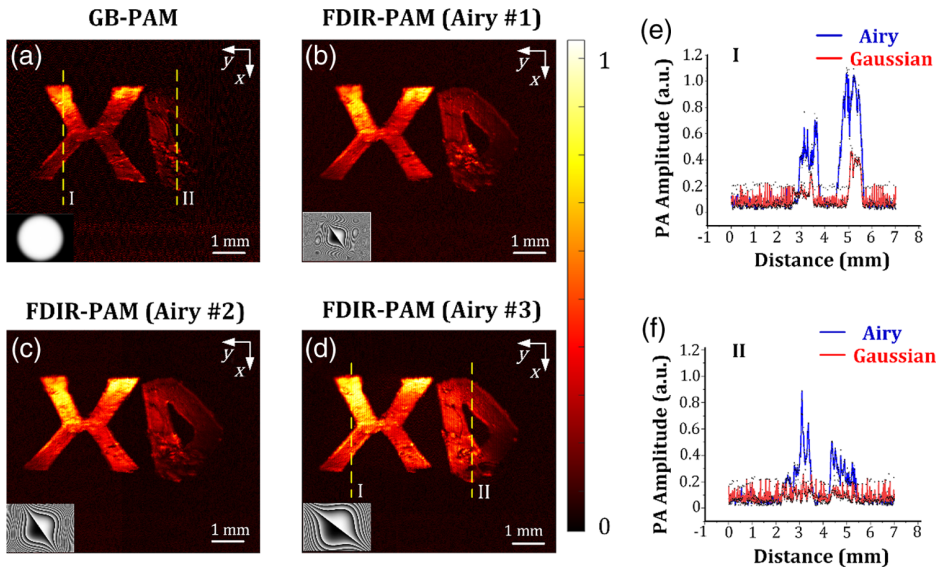

Fig. 3 PAM images of a letter pattern phantom. (a)–(d) Photoacoustic imaging characterization of the letter phantom by Gaussian-beam excitation PAM (GB-PAM) and FDIR-PAM, respectively. The related line profiles at different depths are presented in (e) and (f). Scale bars, 1 mm.

phase patterns onto the SLM. Figures 3(a)–3(d) illustrate the PAM images of the "XD" pattern produced by the four PA excitation beams. In the MAP image of the Gaussian-beam excitation PAM [Fig. 3(a)], only one letter with a clear "X" pattern could be visualized, while the right "D" letter was missed due to the short focal length. When using PA excitation generated from a cubic phase pattern, the elongated DOF of the Airy-beam excitation PAM [Figs. 3(b)–3(d)] allowed for the visualization of both letters, where the dim appearance of the "D" letter can still be captured. Furthermore, when the cubic phase pattern of Airy beam #3 was assigned to the SLM, both "XD" letters were most clearly observed in the FDIR-PAM [Fig. 3(d)], confirming its much larger DOF of at least 2.26 mm. Line profiles at different depths were analyzed to compare the image quality between FDIR-PAM and Gaussian-beam excitation PAM [Figs. 3(e) and 3(f)], demonstrating that the PA images were more resolvable in the former of FDIR-PAM. The increased DOF, combined with consistent lateral resolution throughout the entire mapping volume, could potentially facilitate the characterization of various-layer absorber topology at a micrometer scale. These results indicate the feasibility and superiority of FDIR-PAM, which allows for flexible adjustment of the depth-axial focal length via the incorporation of an SLM.

3.3 Zebrafish Larva and Adult Imaging

The zebrafish is an important model organism that is widely used in neuroscience, cardiovascular research, and other fields because of its transparent development and easy maintenance. The melanin and antholeucin produced by zebrafish are arranged into fixed stripes patterns when they are transported from cells to the surface of the embryo. Hence, it is of utmost importance to study the pigment characterization of zebrafish.

The *in vivo* experiment of zebrafish larvae was first performed to prove the superiority of FDIR-PAM in complex absorption and scattering structure. Two wild-type zebrafish larvae with ~3 mm body lengths at different depths were imaged (1 week old, the Chinese Zebrafish Resource Center). Before imaging, the zebrafish was immobilized on the agarose (1%) at different depths. Figures 4(a) and 4(b) show the structural MAP PAM map results acquired with Gaussian and Airy beams, respectively, given both zebrafishes were roughly caught. Furthermore, zooming in on the yellow boxed regions corresponding to Figs. 4(a) and 4(b) clearly shows that Airy-beam excitation PAM outperformed Gaussian-beam excitation PAM, presenting a high-resolution and deep-resolved zebrafish's head and body with Airy-beam excitation PAM, while the PA signals on the left zebrafish's head and the right fish's body were missing in Gaussian-beam excitation PAM, as shown in Figs. 4(c) and 4(d) and indicated by yellow dashed lines and white arrows. The B-scan images of the dashed line in Figs. 4(c) and 4(d) that correspond to Gaussian-beam excitation PAM and Airy-beam excitation PAM are displayed in Figs. 4(e) and 4(f), respectively. The areas indicated by white arrows are the pupil and head. Obviously, Airy-beam excitation PAM not only characterizes a more comprehensive topology structure of the eyeball but also captures richer depth information on the head structure. In contrast, Gaussian-beam excitation PAM fails to provide this depth information. This experimental results indicated that FDIR-PAM can provide a larger depth range of image detail with the flexibly elongated DOF.

In addition, an experiment was conducted to characterize adult zebrafish *in vivo*, as their pigment pattern formation provides valuable insights into adult form development and evolution.[34] Pigment patterns in zebrafish serve as highly accessible characteristics for studying the cellular basis of the adult form, as microscopic imaging allows visualization of the cells responsible for diverse patterns during development. Leveraging the strong absorption of visible light by pigmentation, label-free 532 nm Gaussian beam excitation PAM proves convenient for acquiring pigment pattern images without excessive sample operation preparation. However, when it comes to imaging irregular topology surfaces with high resolution, conventional Gaussian-beam excitation PAM encounters challenges in accurately characterizing pigment patterns on the fish body. To demonstrate the comprehensive benefits of FDIR-PAM in pigment pattern characterization, a comparison was made between Gaussian-beam excitation PAM and Airy-beam excitation PAM while imaging the adult zebrafish's marginal areas with irregular topology surfaces. Prior to imaging, the adult zebrafish was placed under general anesthesia (tricaine: 0.5 to 1.9 mg/ml), and its body temperature was maintained at 28°C using a thermostatic water tank to ensure motionlessness during the imaging process. The Gaussian-beam excitation PAM image of a 3-month-old adult zebrafish body [Fig. 4(g)] exhibits blurred edges and indistinct pigmented textures in the close-up image. Moreover, important pattern details are missing, as highlighted by the yellow box in Fig. 4(g). These limitations can be attributed to the restricted DOF and significant height fluctuations on the body surface [Fig. 4(i)]. The brighter stripe in Fig. 4(g) represents the regions around the optical focal plane of Gaussian-beam excitation PAM, which exhibit better signal-to-noise ratio and resolution compared to the out-of-focus regions. In contrast, the Airy-beam excitation PAM image of the zebrafish body [Fig. 4(h)] showcases well-resolved texture features of pigment patterns that are not discernible in the Gaussian-beam excitation PAM image, as indicated by the white arrow. The close-up image shown in Fig. 4(h) clearly exhibits distinct pigment patterns, whereas the corresponding region of interest in the Gaussian-beam excitation PAM image appears blurred or even absent, as denoted by the asterisk (*) in the relevant areas [Fig. 4(j)]. Furthermore, a comparison of the cross-sectional images obtained from the respective dotted lines in Figs. 4(g) and 4(h) unequivocally demonstrates the superiority of Airy-beam excitation PAM in characterizing pigment patterns. This advantage becomes particularly evident when dealing with the uneven surface of the fish body, which possesses an irregular topology structure and necessitates a substantial DOF. To further facilitate a quantitative comparison, it is important to consider the contrast, which closely relates to the signal-to-background ratio (SBR) and profoundly impacts spatial resolution. A markedly high SBR, coupled with a superior FWHM, signifies the detail-resolving capability. Consequently, in Fig. 4(m), the measured FWHMs of (I), (II), (III), and (IV) [marked by green dashed lines in (a), (b), (e), (f), (i), and (j)] obtained through Gaussian PAM were 164.6 μm, unmeasurable, and 40.6 μm, respectively. However, with the implementation of FDIR-PAM, the corresponding FWHMs decreased to 87.3, 34.9, and 34.6 μm, affirming a significant improvement in lateral and axial resolving capabilities using Airy-beam excitation PAM. Simultaneously, the SRS profile of (IV) exhibited better signal-to-noise performance with Airy beam imaging, indicating that pigmented streaks present in deeper regions of fish

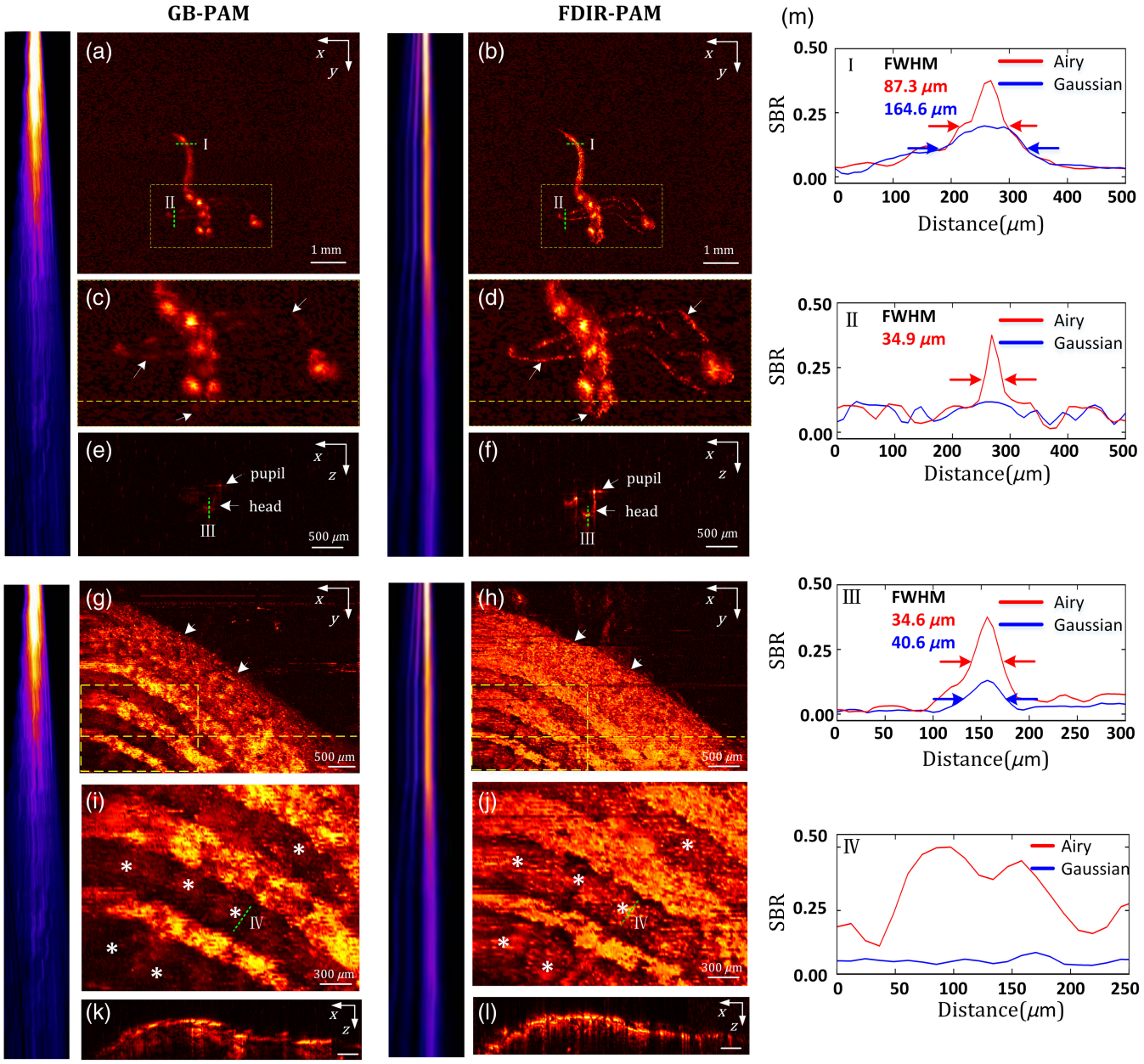

Fig. 4 *In vivo* PAM characterization of zebrafishes, larvae and adults. (a) and (b) PAM images of two zebrafish larvae via Gaussian-beam excitation PAM (GB-PAM) and FDIR-PAM. (c) and (d) Zoom-in *en face* maps that correspond to the yellow boxes of (a) and (b), respectively. (e) and (f) Cross-sectional maps that correspond to the dashed lines in (c) and (d). (g) and (h) PAM images of zebrafish adult fish body using the Gaussian and Airy beams. (i) and (j) Zoom-in *en face* maps that correspond to yellow boxes of (g) and (h), respectively. (k) and (l) Cross-sectional maps that correspond to the dashed lines in (g) and (h). (m) Intensity profiles along the lines depicted in (I), (II), (III), and (IV).

bodies can be effectively detected using FDIR-PAM, which offers a greater DOF.

3.4 In Vivo Mouse Brain Imaging

Eventually, with the capability of revealing structural and functional information in a label-free manner, Gaussian-beam excitation PAM in visible light has been widely used to characterize both the brain vasculature morphology, blood flow, oxygen saturation, and oxygen metabolism function. However, the pronounced curvature of the mouse brain cortex can hinder the high-resolution mapping of the comprehensive cerebral vessels to some extent. To showcase the advantages of FDIR-PAM in characterizing *in vivo* brain vasculature, we performed imaging on a mouse brain with an intact skull. Prior to the experiments, the scalp of a 4-week-old BALB/c female mouse was meticulously prepared, exposing the intact skulls and creating a region of interest measuring 4 mm × 2 mm. The mouse was then anesthetized using a diluted solution of chloral hydrate (0.2 g/kg) administered through intraperitoneal injection.

Subsequently, the mouse's head was secured onto a brain stereotactic apparatus to facilitate further coupling operations. All experimental procedures strictly adhered to the protocols approved by the Institutional Animal Care and Use Committee at the Chengdu Dossy Experimental Animal Company. The results revealed that conventional Gaussian-beam excitation PAM in visible light exhibited fewer blood vessels and missed some vessels located around the right edge areas of the mouse brain [Fig. 5(a)]. In contrast, Airy-beam excitation PAM clearly depicted more vessels in these edge areas, exhibiting enhanced resolution even at distances exceeding 1000 μm from the top surface [Fig. 5(b)]. The presence of irregular non-vessel-shaped structures in the upper corner of the images may be attributed to imperfect coupling operation procedures, leading to minor bleeding in the brain. Moreover, multiscale vessel enhancement filtering maps were performed within the region of interest [Figs. 5(c) and 5(d)], encompassing the rectangular dotted line areas in Figs. 5(a) and 5(b). Consequently, it was evident that Airy-beam excitation PAM could accurately identify a

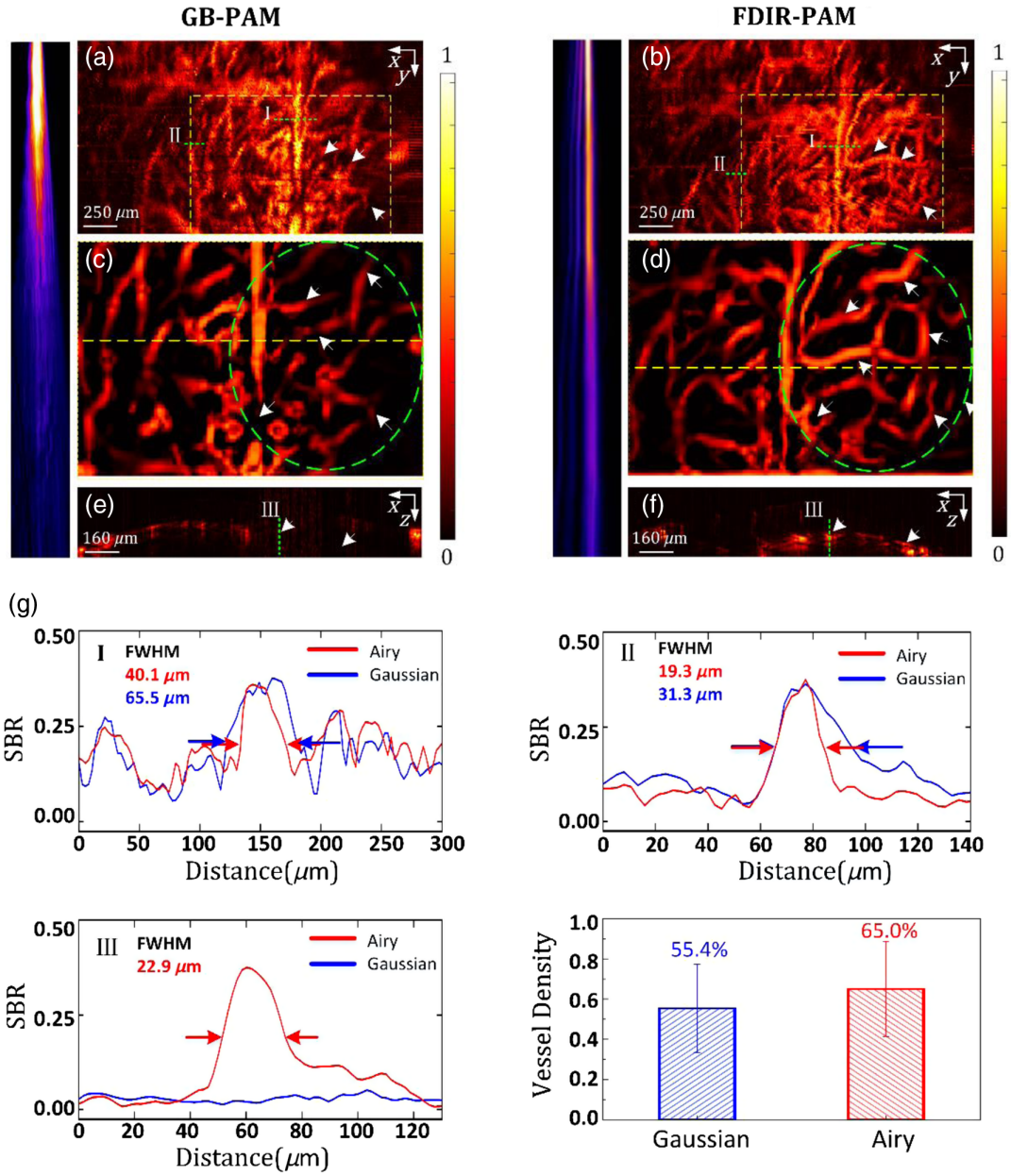

Fig. 5 *In vivo* label-free PAM characterization of the mouse brain. (a) and (b) Imaging of brain vasculature via GB-PAM and FDIR-PAM. (c) and (d) Zoom-in *en face* maps with multiscale vessel enhancement filtering operator that correspond to the yellow boxes of (a) and (b), respectively. (e) and (f) Cross-sectional maps that correspond to the dashed lines of (c) and (d), respectively. FDIR-PAM reveals a greater number of blood vessels surrounding the right-edge areas of the mouse brain compared to conventional GB-PAM. (g) Intensity profiles along the lines depicted in (I), (II), and (III), as well as statistical analysis of vessel density, were conducted to compare GB-PAM and FDIR-PAM.

more comprehensive distribution of vasculature compared to Gaussian-beam excitation PAM, capturing a greater number of vessels (indicated by the white arrow mark within the oval area with dotted green lines). The B-scan images in Figs. 5(e) and 5(f) depict the dashed lines corresponding to Gaussian-beam excitation PAM and Airy-beam excitation PAM, respectively. Due to slight animal movement during the imaging process, the two B-scan lines did not align perfectly. Nevertheless, this discrepancy further confirmed the DOF extension capability in the depth direction. Furthermore, through the analysis of SBR intensity at specific locations of interest (I, II, III), it became evident that Airy-beam excitation PAM exhibited superior vascular-resolving capabilities, with FWHM values of 40.1 versus 65.5 μm and 19.3 versus 31.3 μm for Airy-beam and Gaussian-beam excitation PAMs, respectively. Particularly in the axial direction, Airy-beam excitation PAM clearly captured vessel details with an FWHM of 22.9 μm that were undetectable by Gaussian-beam excitation PAM (III). Following a comprehensive statistical analysis of zebrafish larvae, zebrafish adults, and cerebral vasculature, a notable 62% improvement in detail-resolving capability was observed on average using FDIR-PAM compared to Gaussian-beam excitation PAM. Finally, quantitative statistics were performed on vascular density in the boxed region, revealing that FDIR-PAM comprehensively and significantly captured more vasculature network information [Fig. 5(g), $P < 0.05$], thereby demonstrating its ability to extend the DOF for comprehensive vasculature characterization.

4 Discussion

In this study, we successfully developed FDIR-PAM, which utilizes an SLM to generate flexible and adjustable Airy-beam excitation. This innovative approach significantly extends the DOF for high-resolution imaging, making it particularly valuable for *en face* imaging of surfaces with varying topologies or for 3D volumetric imaging. By applying this technique, we were able to overcome the challenge of achieving high-resolution imaging of variable topology surfaces in both zebrafish larvae and adults. This opens up promising avenues for studying pigment pattern formation and understanding the mechanisms behind stripe formation in adult zebrafish. Furthermore, we demonstrated the *in vivo* application of FDIR-PAM in imaging mouse brain vessels, resulting in improved resolution and extended DOF in a label-free model. Importantly, by utilizing the non-diffraction Airy beam, we achieved an impressive ~17-fold improvement in DOF compared to traditional Gaussian-beam excitation PAM methods. Although the index parameters are not as bright as those mentioned in Ref. 19, considering the needs of a series of sinusoidal fringes equipped with complex postprocessing, it is not suitable for the study of rapid real-time monitoring of zebrafish activity as well as functional metabolism in mice microcirculation. The FDIR-PAM could compensate for the limitations of the above application scenarios. The resolution and image quality in this study can be further improved by implementing spatial filtering, optimizing the modulation parameters β, or designing a special phase modulation mask to weaken the influence of sidelobes.[30] By employing these strategies either individually or in combination, we can effectively mitigate the deterioration of resolution and image quality caused by sidelobe effects in practical applications. In order to further optimize beam quality, the influence of sidelobes on imaging quality is alleviated with designed phase modulation, resulting in imaging maps of sidelobe-suppressed Airy beams PAM (Supplementary Material 1, Note 2, and Note 3). In the future, the exceptionally promising DOF results demonstrated by the Airy beam will be potential in the diagnosis of brain diseases and dermatology applications, where a comprehensive characterization covering the flexible DOF of cerebral tissue and skin layer from epidermis to deep vascular plexus is desirable for assisting the doctor's judgment.[35,36] At the same time, it is an attractive tool for the study of model biology of zebrafish development, where revealing cardiovascular phylogeny of cardiovascular phenotypes and hemodynamics in relation to cancer cell migration in long-term growth, as well as characterizing the zebrafish vascular system.[37] The development of multiscale and multispectral FDIR-PAM techniques is beneficial. These techniques can significantly improve the characterization and quantitative analysis of zebrafish biomarkers across different growth stages, leading to a deeper understanding of developmental processes and disease mechanisms. Moreover, this technique holds great potential for enhancing the limited DOF of PAMs that typically utilize high numerical aperture (NA) objectives, particularly in atherosclerosis applications, where increased DOF would enable comprehensive identification of lipid and intraplaque hemorrhage. In addition, in the case of ultrahigh-resolution PAMs that utilize tightly focused Gaussian beams, the DOF is considerably smaller compared to the penetration depth. To address this limitation, a more favorable approach would be to combine the Airy beam with multi-focus image fusion or a two-stage deep-learning network in a hardware-plus-algorithm joint configuration.[38–40] This enables the characterization of a broader range of topological structure changes across different scales and wavelength ranges, including scenarios with high NA and short wavelengths. Hardware-plus-algorithm-based FDIR-PAM can achieve improved imaging robustness and versatility, advancing research in various biomedical and life science fields. The development of symmetric Airy beams can further offer several advantages in FDIR-PAM, leading to improved modulation efficiency, sensitivity of photoacoustic signal sensing, and enhanced image contrast. This is due to the symmetrical superposition of beam intensity of symmetric Airy beams. Finally, when considering clinical translation in the future, incorporating phase masks as replacements for SLMs can significantly reduce system complexity and cost in the context of translating FDIR-PAM into clinical applications.

5 Conclusion

In conclusion, we have successfully proposed and validated an FDIR-PAM system that utilizes the nondiffraction Airy beam as the excitation source for photoacoustic signals. By incorporating the Airy beam into PAM, we achieved an impressive extension of the DOF to ~926 μm, which is more than 17 times larger than that of a Gaussian beam. The flexibility in adjusting the focal length further enhances the versatility of the proposed FDIR-PAM system. In addition to imaging mini-type zebrafish larvae, zebrafish adults, and mouse brains, this innovative approach, incorporating SLM, holds immense potential for a wide range of biomedical applications, including the study of skin cancers, brain diseases, and atherosclerosis.

Disclosures

The authors have no conflicts of interest to disclose.

Code and Data Availability

Data underlying the results presented in this paper are not publicly available at this time but may be obtained from the authors upon reasonable request.

Acknowledgments

This work was supported by the National Natural Science Foundation of China (Grant Nos. 62105255 and 62275210), the Xidian University Specially Funded Project for Interdisciplinary Exploration (Grant No. TZJH2024043), the Key Research and Development Program of Shaanxi Province (Grant No. 2023-YBSF-293), the National Young Talent Program and Shaanxi Young Top-notch Talent Program, and the Fundamental Research Funds for CentralUniversities (Grant No. ZYTS23187).

References

1. J. Aguirre et al., "Precision assessment of label-free psoriasis biomarkers with ultra-broadband optoacoustic mesoscopy," *Nat. Biomed. Eng.* **3**(5), 0068 (2017).
2. M. Seeger et al., "Multimodal optoacoustic and multiphoton microscopy of human carotid atheroma," *Photoacoustics* **4**(3), 102–111 (2016).
3. Z. Q. Xu et al., "Visualizing tumor angiogenesis and boundary with polygon-scanning multiscale photoacoustic microscopy," *Photoacoustics* **26**, 100342 (2022).
4. W. Qin et al., "High-resolution *in vivo* imaging of rhesus cerebral cortex with ultrafast portable photoacoustic microscopy," *NeuroImage* **238**, 118260 (2021).
5. X. W. Shen, H. P. Wu, and L. Dong, "Recent advances of photoacoustic imaging technology in biomedicine [Invited]," *Acta Photonica Sin.* **52**(3), 0352105 (2023).
6. A. DiSpirito et al., "Reconstructing undersampled photoacoustic microscopy images using deep learning," *IEEE Trans. Med. Imaging* **40**(2), 562–570 (2021).
7. C. Liu et al., "Five-wavelength optical-resolution photoacoustic microscopy of blood and lymphatic vessels," *Adv. Photonics* **3**(1), 016002 (2021).
8. R. Cao et al., "Optical-resolution photoacoustic microscopy with a needle-shaped beam," *Nat. Photonics* **17**(1), 89–95 (2022).
9. Y. T. Zhao et al., "Ultraviolet metalens for photoacoustic microscopy with an elongated depth of focus," *Opt. Lett.* **48**(13), 3435–3438 (2023).
10. J. Ma et al., "Transparent microfiber Fabry-Perot ultrasound sensor with needle-shaped focus for multiscale photoacoustic imaging," *Photoacoustics* **30**, 100482 (2023).
11. T. Ralston et al., "Interferometric synthetic aperture microscopy," *Nat. Phys.* **3**(2), 129–134 (2007).
12. A. Descloux et al., "Combined multi-plane phase retrieval and super-resolution optical fluctuation imaging for 4D cell microscopy," *Nat. Photonics* **12**(7), 438 (2018).
13. S. Geissbuehler et al., "Live-cell multiplane three-dimensional super-resolution optical fluctuation imaging," *Nat. Commun.* **5**, 5830 (2014).
14. S. Abrahamsson et al., "Fast multicolor 3D imaging using aberration-corrected multifocus microscopy," *Nat. Methods* **10**(1), 60–63 (2013).
15. G. A. Zhang, R. Horstmeyer, and C. H. Yang, "Wide-field, high-resolution Fourier ptychographic microscopy," *Nat. Photonics* **7**(9), 739–745 (2013).
16. B. Park et al., "Reflection-mode switchable subwavelength Bessel-beam and Gaussian-beam photoacoustic microscopy *in vivo*," *J. Biophotonics* **12**(2), e201800215 (2019).
17. B. W. Jiang, X.Q. Yang, and Q. M. Luo, "Reflection-mode Bessel-beam photoacoustic microscopy for *in vivo* imaging of cerebral capillaries," *Opt. Express* **24**(18), 20167–20176 (2016).
18. J. H. Shi et al., "Bessel-beam Grueneisen relaxation photoacoustic microscopy with extended depth of field," *J. Biomed. Opt.* **20**(11), 116002 (2015).
19. J. M. Yang et al., "Motionless volumetric photoacoustic microscopy with spatially invariant resolution," *Nat. Commun.* **8**(1), 780 (2017).
20. M. Amjadian et al., "Super-resolution photoacoustic microscopy using structured-illumination," *IEEE Trans. Med. Imaging* **40**(9), 2197–2207 (2021).
21. X. L. Chen et al., "Stimulated Raman scattering signal generation in a scattering medium using self-reconstructing Bessel beams," *Photonics Res.* **8**(6), 929–939 (2020).
22. Y. C. Hu et al., "Extended depth-of-field all-optical photoacoustic microscopy with a dual non-diffracting Bessel beam," *Opt. Lett.* **44**(7), 1634–1637 (2019).
23. W. Song et al., "Flexibly adjustable depth-of-focus photoacoustic microscopy with spatial light modulation," *Appl. Phys. Lett.* **113**(16), 163502 (2018).
24. K. S. Lee and L. P. Rolland, "Bessel beam spectral-domain high-resolution optical coherence tomography with micro-optic axicon providing extended focusing range," *Opt. Lett.* **33**(15), 1696–1698 (2008).
25. G. A. Siviloglou et al., "Observation of accelerating Airy beams," *Phys. Rev. Lett.* **99**(21), 213901 (2007).
26. T. Vettenburg et al., "Light-sheet microscopy using an Airy beam," *Nat. Method* **11**(5), 541–544 (2014).
27. P. F. Liu et al., "Airy beam assisted NIR-II light-sheet microscopy," *Nano Today* **47**, 101628 (2022).
28. N. R. Subedi et al., "Airy light-sheet Raman imaging," *Opt. Express* **29**(20), 31941–31951 (2021).
29. M. Zhang, Z. J. Ren, and P. Yu, "Improve depth of field of optical coherence tomography using finite energy Airy beam," *Opt. Lett.* **44**(12), 3158–3161 (2019).
30. J. Wang et al., "Airy-beam tomographic microscopy," *Optica* **7**(7), 790–793 (2020).
31. X. L. Song et al., "Airy-beam large volumetric photoacoustic microscopy," https://doi.org/10.48550/arXiv.2011.01152 (2020).
32. G. A. Siviloglou and D. N. Christodoulides, "Accelerating finite energy Airy beams," *Opt. Lett.* **32**(8), 979–981 (2007).
33. Z. Cai et al., "Generation of colorful Airy beams and Airy imaging of letters via two-photon processed cubic phase plates," *Opt. Lett.* **43**(5), 1151–1154 (2018).
34. L. B. Patterson and D. M. Parichy, "Zebrafish pigment pattern formation: insights into the development and evolution of adult form," *Annu. Rev. Genet.* **53**, 505–530 (2019).
35. T. T. W. Wong et al., "Label-free automated three-dimensional imaging of whole organs by microtomy-assisted photoacoustic microscopy," *Nat. Commun.* **8**(1), 1386 (2017).
36. A. Sahu et al., "Evaluation of a combined reflectance confocal microscopy-optical coherence tomography device for detection and depth assessment of basal cell carcinoma," *JAMA Dermatol.* **154**(10), 1175–1183 (2018).
37. A. Bensimon-Brito et al., "Integration of multiple imaging platforms to uncover cardiovascular defects in adult zebrafish," *Cardiovasc. Res.* **118**(12), 2665–2687 (2022).
38. Y. Zhang et al., "Multi-focus light-field microscopy for high-speed large-volume imaging," *PhotoniX* **3**(1), 30 (2022).
39. W. T. Zhou et al., "Multi-focus image fusion with enhancement filtering for robust vascular quantification using photoacoustic microscopy," *Opt. Lett.* **47**(15), 3732–3735 (2022).
40. J. Meng et al., "Depth-extended acoustic-resolution photoacoustic microscopy based on a two-stage deep learning network," *Biomed. Opt. Express* **13**(8), 4386–4397 (2022).

Biographies of the authors are not available.